RSC Advances

PAPER

View Article Online
View Journal | View Issue

Cite this: *RSC Adv.*, 2026, **16**, 29867

Design, synthesis, and biological evaluation of novel imidazole–morpholinone hybrids as broad-spectrum antimicrobial agents: molecular docking, DFT, and ADMET studies

Amrish J. Dave, [ab] Sweta S. Joshi, *[a] Jay B. Maheta, [c] Yogesh O. Bhola *[c] and Jatin Upadhyay[a]

A novel series of five imidazole–morpholinone hybrid compounds (**10a–e**) was designed, synthesised, and evaluated as broad-spectrum antimicrobial agents. The target molecules integrate a 5-formyl-1-butylimidazole core, a (3-oxomorpholin-4-yl)phenyl pharmacophore, and variable C5-aryl groups introduced *via* late-stage Suzuki–Miyaura cross-coupling, assembled through a concise five-step convergent route. All compounds were characterised by $^{1}H/^{13}C$ NMR, IR, and HR-ESI-MS. *In vitro* antimicrobial evaluation against four bacterial (*S. aureus*, *S. pyogenes*, *E. coli*, *P. aeruginosa*) and two fungal (*C. albicans*, *A. niger*) strains revealed compound **10c** as the most potent analogue, matching chloramphenicol (MIC 7.81 μg mL^{-1}) and griseofulvin (MIC 15.62 μg mL^{-1}) reference standards. Molecular docking against *S. aureus* DNA gyrase (2XCT) and *E. coli* GyrB24 (7P2M), corroborated by DFT analysis (B3LYP/6-311++G(d,p)) and ADMET profiling, confirmed DNA gyrase inhibition as the primary mechanism and established **10c** as a promising drug-like lead for further development.

Received 19th April 2026
Accepted 24th May 2026

DOI: 10.1039/d6ra03352k

rsc.li/rsc-advances

Introduction

Antimicrobial resistance (AMR) is a critical global health threat, with the WHO projecting up to 10 million annual deaths by 2050.[1,2] The dwindling pipeline of structurally novel antibacterial and antifungal agents makes the discovery of new chemotypes an urgent scientific priority.[3,4]

Heterocyclic scaffolds underpin modern drug discovery, comprising over 85% of approved small-molecule drugs. The imidazole ring is particularly privileged, offering bioisosteric versatility, hydrogen-bond donor/acceptor duality, and metal-chelating ability.[5–7] Its clinical utility is well demonstrated across diverse therapeutic areas, metronidazole and tinidazole (antibacterial/antiprotozoal), ketoconazole and fluconazole (antifungal), losartan (antihypertensive), and omeprazole (proton-pump inhibitor), confirming that the C2 and C4/C5 positions are highly amenable to structural diversification.[8–11]

The morpholin-3-one motif complements this scaffold as a six-membered lactam–ether hybrid that mimics peptide-bond geometry while enhancing aqueous solubility and metabolic stability.[12–15] Its presence in rivaroxaban, linezolid, and aprepitant highlights its capacity to engage diverse biological targets. Hybridisation of the imidazole nucleus with a morpholinone moiety *via* a suitable tether therefore represents a rational strategy for accessing compounds with multifaceted antimicrobial potential.[16–18] (Fig. 1).

Transition-metal-catalysed cross-coupling, particularly the Suzuki–Miyaura reaction, has become indispensable in pharmaceutical synthesis owing to its functional-group tolerance, mild conditions, and ready access to a wide range of arylboronic acids.[19–21] The prevalence of biaryl pharmacophores in drugs such as losartan, valsartan, and voriconazole underscores the biological value of this connectivity.[22,23]

The present series integrates three pharmacophoric elements: (i) a 5-formyl-1-butylimidazole core for lipophilicity and condensation chemistry; (ii) a (3-oxomorpholin-4-yl) phenyl segment to emulate rivaroxaban-type hydrogen-bonding with bacterial targets; and (iii) a variable C5-aryl group introduced *via* Suzuki coupling for systematic SAR exploration. An acetamide linker (–OCH_2CONH–) bridges both pharmacophores, preserving conformational flexibility and hydrogen-bonding capacity.[24–27]

Literature precedent supports this design: 4-substituted imidazoles exhibit MIC values of 25–200 μg mL^{-1} against ESKAPE pathogens, while *N*-arylacetamide-tethered morpholinones inhibit FtsZ and DNA gyrase. Merging these fragments

[a]*Department of Chemistry, Matushri Virbaima Mahila Science & Home Science College-Rajkot, Gujarat, India. E-mail: swetajoshi.chem@gmail.com*

[b]*Department of Chemistry, M. P. Shah Arts and Science College-Surendranagar, Gujarat, India*

[c]*Department of Chemistry, Shri M.P. Pandya Science College-Lunawada, Shri Govind Guru University-Godhra, Gujarat, India. E-mail: dryobhola@gmail.com; yogeshbhola90@gmail.com*

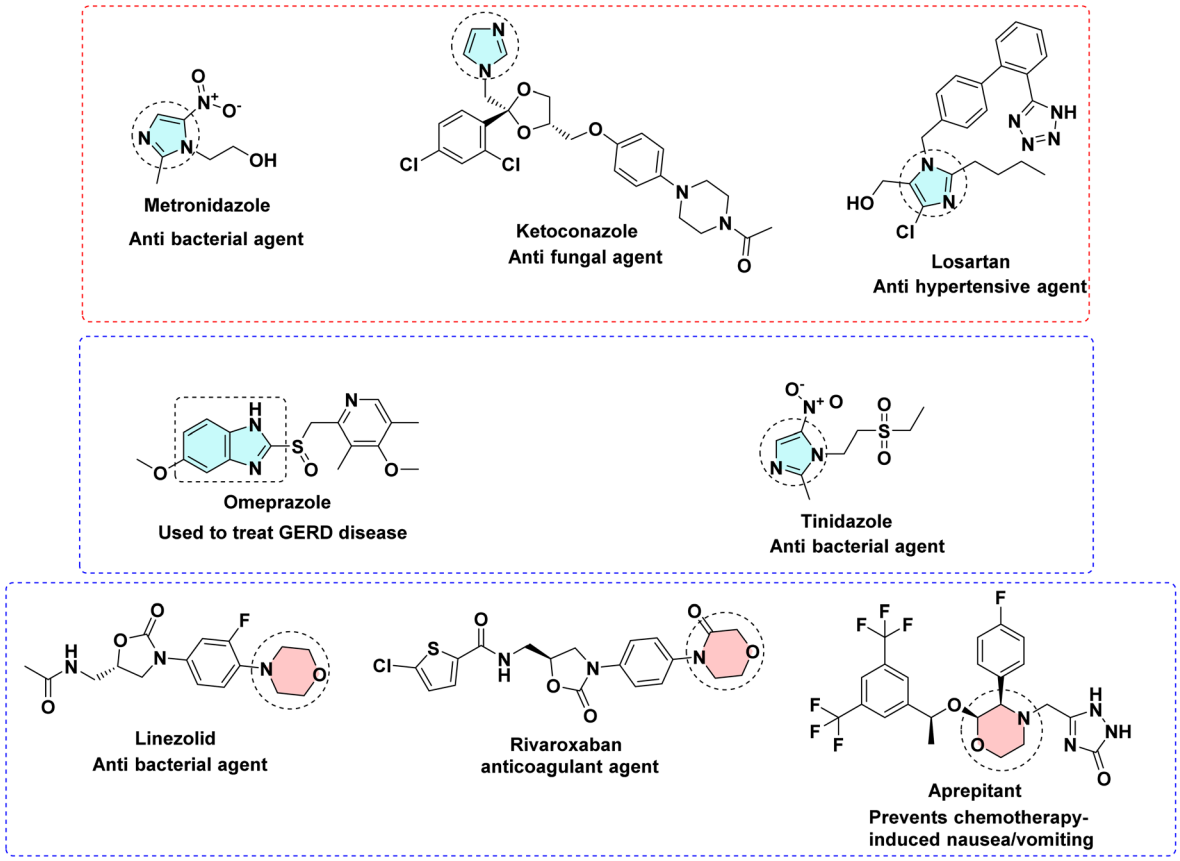

Fig. 1 Structural design rationale for the target imidazole–morpholinone hybrids (**10a–e**), illustrating the pharmacophoric integration of the 5-formyl-1-butylimidazole core, the (3-oxomorpholin-4-yl)phenyl segment, and the variable C5-aryl group connected *via* an acetamide tether.

was therefore hypothesised to afford synergistic antimicrobial activity.

Herein we report the five-step convergent synthesis of compounds **10a–e** alongside spectroscopic characterisation, *in vitro* antimicrobial evaluation, molecular docking (DNA gyrase B, PDB: 2XCT; FtsZ, PDB: 7P2M), DFT analysis (B3LYP/6-31G*), and ADMET profiling to establish a comprehensive SAR framework.

Result & discussion

The target compounds **10a–e** were assembled *via* a concise, modular synthetic route featuring imidazole formation, regioselective *N*-alkylation, and late-stage Suzuki–Miyaura diversification (Scheme 1). The synthesis commenced with a Pinner reaction of valeronitrile (**1**) under anhydrous HCl in methanol at 0–5 °C, affording imidate hydrochloride **2** in high yield while suppressing ester formation. Subsequent treatment of **2** with glycine (**3**) under Vilsmeier–Haack conditions ($POCl_3$/DMF) enabled a one-pot cyclodehydration–formylation sequence, delivering the key intermediate **4** (4-chloro-5-formylimidazole scaffold). The formation of **4** was confirmed by the diagnostic aldehydic resonance (~9.7 ppm, ^{1}H NMR), consistent with analogous systems. In parallel, chloroacetamide **7** was obtained *via* controlled acylation of 4-(3-oxomorpholin-4-yl)aniline (**5**) with chloroacetyl chloride (**6**) at low temperature, thereby ensuring selective monoacylation. The key *N*-alkylation between **4** and **7** proceeded efficiently using K_2CO_3 in acetonitrile, furnishing intermediate **8** with high N1 regioselectivity, as supported by NOESY correlations. This preference is rationalized by the enhanced nucleophilicity of N1 induced by the electron-withdrawing C4-chloro substituent. Final diversification was achieved through Suzuki–Miyaura cross-coupling of heteroaryl chloride **8** with arylboronic acids (**9a–e**) using $Pd(dppf)Cl_2/K_2CO_3$ in dioxane–water at 100 °C. Despite the inherent reluctance of aryl chlorides toward oxidative addition, the electron-rich dppf ligand facilitated efficient C–C bond formation, affording **10a–e** in 78–89% yields (Fig. 2). Electron-rich boronic acids exhibited higher coupling efficiency, consistent with facilitated transmetalation. Overall, this strategy highlights the synthetic utility of Vilsmeier-enabled imidazole assembly and Pd-catalyzed cross-coupling of heteroaryl chlorides, providing a flexible platform for late-stage functionalization and rapid analogue generation relevant to medicinal chemistry exploration.

Molecular docking results

Molecular docking was performed against two validated bacterial DNA gyrase crystal structures: *S. aureus* DNA gyrase (PDB: 2XCT) and *E. coli* GyrB24 (PDB: 7P2M). Novobiocin served as the

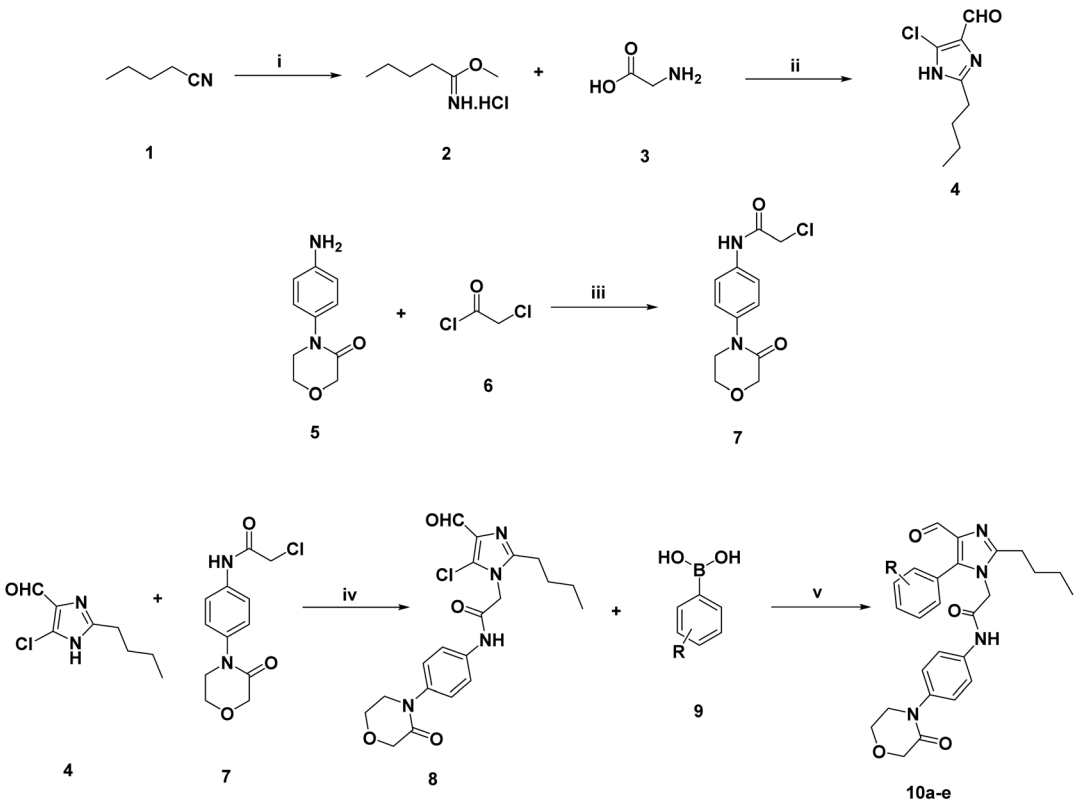

Reagent & Conditions: **(i) HCl, MeOH, 0-5°C; (ii) DMF, $POCl_3$; (iii) Acetone, 0-5°C, 2-3 h; (iv) ACN, K_2CO_3, Reflux, 4-5h; (v) $PdCl_2(dppf)$, K_2CO_3, 100°C, 3h, Dioxane:H_2O**

Scheme 1 Synthetic route to target imidazole derivatives **10a–e** *via* Pinner reaction, Vilsmeier–Haack cyclisation, regioselective *N*-alkylation, and Suzuki–Miyaura cross-coupling.

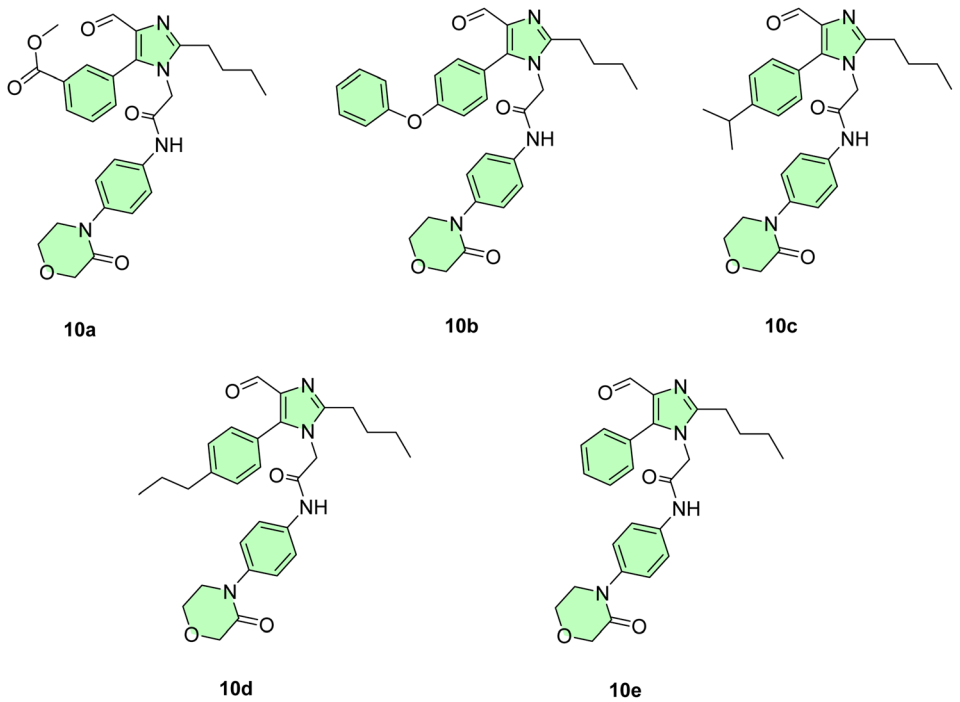

Fig. 2 Chemical structures of the synthesised imidazole–morpholinone hybrid derivatives **10a–e**.

GyrB-specific reference standard for both targets, given its well-established ATP-competitive inhibition of the GyrB ATPase domain. All five synthesised compounds (**10a–e**) exhibited competitive binding affinities, with several surpassing the reference standard for both targets.

S. aureus DNA gyrase (2XCT)

The docking scores against 2XCT ranged from −5.308 to −6.533 kcal mol^{-1}, with compounds **10b** and **10c** surpassing novobiocin (−5.7223 kcal mol^{-1}) by 2.1% and 14.2% respectively, while **10d** showed comparable affinity, and **10a** and **10e** recorded scores below the reference standard. Compound **10c** achieved the highest binding affinity (−6.533 kcal mol^{-1}), driven by an extensive interaction network of 28 total contacts, the largest among all tested compounds. This included 14 hydrophobic residue engagements (TRP 592, LEU 1298, VAL 1302, MET 1113, ALA 588, PHE 1097, PHE 1110, ALA 1094, and others), 2 hydrogen bonds (LYS 1270 backbone, PHE 1110 sidechain), a dense negatively charged network spanning 5 residues (ASP 1294, ASP 589, ASP 448, ASP 1114, ASP 1116), and 4 GLY-backbone contacts providing multidirectional stabilisation within the ATP-binding pocket (Table 1).

Compound **10b** ranked second (−5.842 kcal mol^{-1}) with 12 hydrophobic contacts and a similar charged-residue architecture to **10c**, while **10d** (−5.712 kcal mol^{-1}) is notable for carrying the most hydrophobic interactions (16 contacts) alongside a unique Pi-cation interaction with ARG 1092, indicating aromatic ring engagement within the binding cleft. Compound **10a** (−5.308 kcal mol^{-1}), despite the lowest score in the series, still engages meaningful binding contacts and forms the most H-bond contacts (**4**), engaging ARG 1299, ARG 447, LYS 1270 (backbone), and SER 445 (backbone), suggesting a hydrogen-bond-rich binding mode.

E. coli GyrB24 (7P2M)

Against 7P2M, docking scores spanned −4.582 to −5.821 kcal mol^{-1}. The reference compound novobiocin scored −5.192 kcal mol^{-1}. Compound **10c** again led the series (−5.821 kcal mol^{-1}), exceeding novobiocin by ∼12.1%, with 15 hydrophobic contacts across a well-conserved binding site (VAL 43, ALA 47, VAL 71, ILE 78, PRO 79, MET 166, VAL 167, VAL 120, TYR 109 and others) and a broad negatively charged environment (ASP 49, ASP 73, GLU 50, ASP 106). The consistent H-bond to ARG 76 backbone was observed in compounds **10a–c** and **10e**, while **10d** engaged THR 165 backbone instead, reflecting a subtle shift in binding geometry, possibly attributable to structural differences in substituents.

Compound **10d** (−5.546 kcal mol^{-1}) ranks second against 7P2M, surpassing the novobiocin benchmark, with 16 hydrophobic contacts and the widest polar engagement, including GLN 72, HIS 99, ASN 46, SER 108. Compound **10b** (−4.918 kcal mol^{-1}) forms the most contacts (24) in its score bracket, indicating efficient packing within the binding groove despite its moderate affinity. Compound **10a** recorded the lowest affinity in this target (−4.582 kcal mol^{-1}) yet still engages a structurally meaningful set of residues comparable to higher-scoring analogues, suggesting partial occupancy of the binding site (Table 2).

Across both targets, a clear pattern emerges: **10c** > **10d** > **10b** > **10e** > **10a** in terms of overall binding potency. The convergence of strong scores on both structurally distinct gyrase targets is indicative of genuine inhibitory potential rather than a target-specific artefact.

Antimicrobial activity

All compounds were evaluated for minimum inhibitory concentration (MIC) by the broth microdilution method against four bacteria, *S. aureus* MTCC 96, *S. pyogenes* MTCC 442, *E. coli* MTCC 443, *P. aeruginosa* MTCC 1688 and two fungi, *C. albicans* MTCC 227 and *A. niger* MTCC 282. Chloramphenicol (bacterial standard) and griseofulvin (fungal standard) served as references.

Compound **10c** demonstrated the strongest and most consistent antibacterial profile across all four organisms. Against *S. aureus*, **10c** recorded a MIC of 7.81 μg mL^{-1}, essentially equivalent to the chloramphenicol standard (7.8 μg mL^{-1}), making it the sole test compound to match reference-level activity. Against *S. pyogenes*, **10c** again matched the standard (7.82 *vs.* 7.8 μg mL^{-1}). For Gram-negative pathogens *E. coli* and *P. aeruginosa*, **10c** returned MIC values of 15.62 μg mL^{-1} each, ranked best among all synthesised compounds for these organisms. This dual Gram-positive/Gram-negative potency, particularly against the inherently resistant *P. aeruginosa*, underlines the broad-spectrum utility of **10c**.

Compound **10a** showed remarkable activity against *P. aeruginosa* (MIC 7.82 μg mL^{-1}), equalling the chloramphenicol standard, which is noteworthy given the organism's intrinsic resistance mechanisms. However, **10a** was relatively inactive against *S. pyogenes* (62.5 μg mL^{-1}) and *A. niger* (62.5 μg mL^{-1}), indicating a narrower spectrum. Compound **10b** performed best against *S. pyogenes* (15.62 μg mL^{-1}) and *A. niger* (31.25 μg mL^{-1}), but was comparatively weak against *E. coli* (62.5 μg mL^{-1}). Compounds **10d** and **10e** exhibited moderate-to-good activity against Gram-positive organisms (15.62 μg mL^{-1} for *S. aureus* and *S. pyogenes* for **10d**) but weak activity against Gram-negative rods and fungi, suggesting diminished membrane permeability with increasing structural bulk.

Among the compounds, **10c** exhibited the best antifungal potency, with an MIC of 15.62 μg mL^{-1} against both *C. albicans* and *A. niger*, matching the griseofulvin standard (15.62 μg mL^{-1}) exactly. Compound **10b** achieved 62.5 μg mL^{-1} *vs. C. albicans* but 31.25 μg mL^{-1} *vs. A. niger*, showing moderate differential activity between the two fungal species. Compounds **10d** and **10e** were inactive at the concentrations tested (MICs of 62.5 μg mL^{-1} for both fungi), suggesting that their structural features are incompatible with fungal membrane or cell wall targets.

The data establish a clear SAR trend. Compound **10c** occupies the optimal activity profile, the most electronically rich and sterically balanced analogue, achieving excellent MIC values across all six organisms. Its superiority correlates directly with its docking performance: the highest binding affinity in

Table 1 Molecular docking scores (kcal mol^{-1}), binding poses, hydrophobic/polar interactions, hydrogen-bond interactions, and charged/glycine backbone contacts of compounds **10a–e** and reference drug novobiocin against *Staphylococcus aureus* DNA gyrase (PDB: 2XCT)

Staphylococcus aureus DNA gyrase (2XCT)					
Compound code	Docking score (kcal mol^{-1})	Docking image	Hydrophobic interactions/ Polar interactions	H-bond interactions	Others (charged/GLY)
10a	−5.308	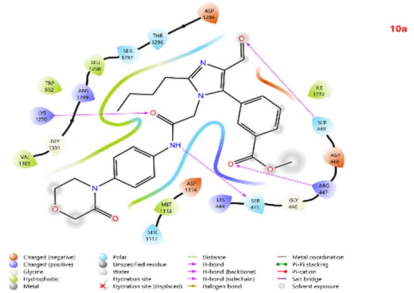	TRP 592, LEU 1298, VAL 1302, MET 1113, ILE 1274, THR 1296, SER 1297, SER 449, SER 445, SER 1112	LYS 1270 (backbone), ARG 1299 (backbone), ARG 447 (sidechain), SER 445 (backbone)	ARG 1299, ARG 447, LYS 1270 (charged+); ASP 1294, ASP 448, ASP 1114 (charged−); GLY 1301, GLY 446
10b	−5.842	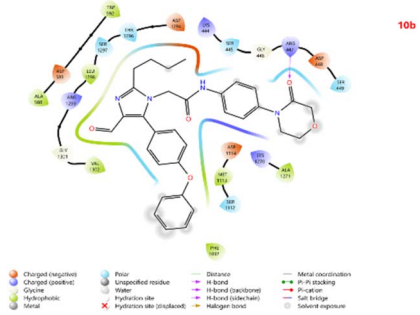	TRP 592, LEU 1298, VAL 1302, MET 1113, ALA 588, ALA 1271, PHE 1097, THR 1296, SER 1297, SER 449, SER 445, SER 1112	ARG 447 (sidechain)	ARG 1299, ARG 447, LYS 1270 (charged+); ASP 1294, ASP 589, ASP 448, ASP 1114 (charged−); GLY 1301, GLY 446
10c	−6.533	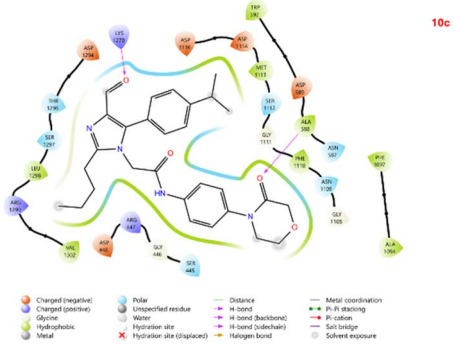	TRP 592, LEU 1298, VAL 1302, MET 1113, ALA 588, PHE 1097, PHE 1110, ALA 1094, THR 1296, SER 1297, SER 445, SER 1112, ASN 587, ASN 1109	LYS 1270 (backbone), PHE 1110 (sidechain)	ARG 1299, ARG 447, LYS 1270 (charged+); ASP 1294, ASP 589, ASP 448, ASP 1114, ASP 1116 (charged−); GLY 1301, GLY 446, GLY 1111, GLY 1108
10d	−5.712		PHE 1097, VAL 1091, MET 1113, TYR 1087, PHE 1266, ILE 1264, ALA 1118, ALA 1119, ALA 1120, MET 1121,	ARG 1272 (backbone); Pi-cation: ARG 1092	ARG 1272, ARG 1092, LYS 1270 (charged+); ASP 1116, GLU 1088

Table 1 (*Contd.*)

Staphylococcus aureus DNA gyrase (2XCT)					
Compound code	Docking score (kcal mol^{-1})	Docking image	Hydrophobic interactions/ Polar interactions	H-bond interactions	Others (charged/GLY)
		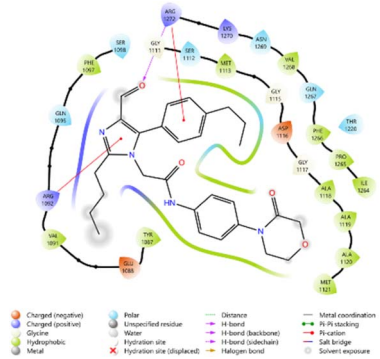 10d	VAL 1268, PRO 1265, SER 1098, SER 1112, GLN 1095, GLN 1267		(charged−); GLY 1111, GLY 1115, GLY 1117
10e	−5.658	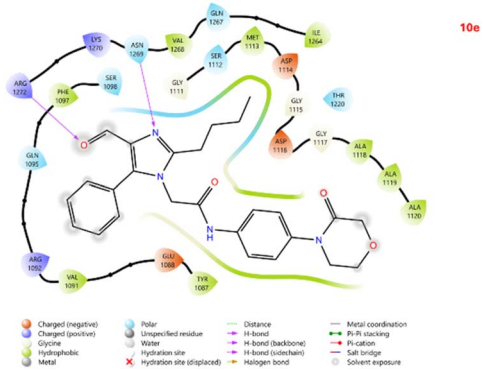 10e	VAL 1268, MET 1113, ILE 1264, PHE 1097, VAL 1091, TYR 1087, ALA 1118, ALA 1119, ALA 1120, SER 1098, SER 1112, GLN 1267, ASN 1269, THR 1220	ASN 1269 (backbone), ARG 1272 (sidechain)	ARG 1272, ARG 1092, LYS 1270 (charged+); ASP 1114, ASP 1116, GLU 1088 (charged−); GLY 1111, GLY 1115, GLY 1117
Novobiocin	−5.7223	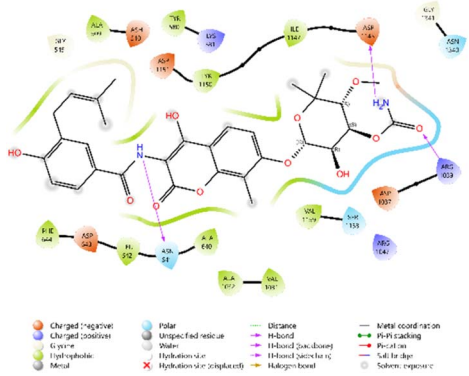	ALA 509, TYR 580, ALA 640, LEU 642, PHE 644, ALA 1032, VAL 1031, ILE 1147, TYR 1150, VAL 1159	ASN 641 backbone), ARG 1039 (backbone), ASP 1145 (backbone)	LYS 581, ARG 1039, ARG 1047, (charged+); ASH 510, ASP 643, ASP 1037, ASP 1151, ASP 1145, (charged−)

Table 2 Molecular docking scores (kcal mol^{-1}), binding poses, hydrophobic/polar interactions, hydrogen-bond interactions, and charged/glycine backbone contacts of compounds **10a–e** and reference drug novobiocin against *Escherichia coli* GyrB24 (PDB: 7P2M)

Escherichia coli DNA gyrase subunit B (GyrB24) (7P2M)					
Compound code	Docking score (kcal mol^{-1})	Docking image	Hydrophobic interactions/ Polar interactions	H-bond interactions	Others (charged/GLY)
10a	−4.582	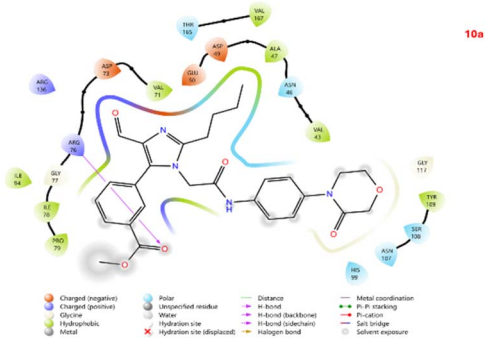	VAL 167, ALA 47, VAL 43, ILE 94, ILE 78, PRO 79, TYR 109, THR 165, ASN 46, HIS 99, SER 108, ASN 107	ARG 76 (backbone)	ARG 136, ARG 76 (charged+); ASP 49, ASP 73, GLU 50 (charged−); GLY 77, GLY 117
10b	−4.918	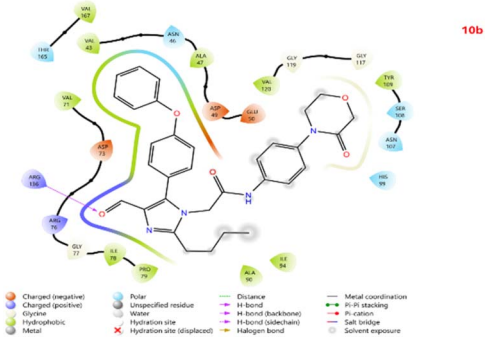	VAL 167, VAL 43, ALA 47, VAL 71, ILE 78, PRO 79, ILE 94, ALA 90, TYR 109, VAL 120, THR 165, ASN 46, HIS 99, SER 108, ASN 107	ARG 76 (backbone)	ARG 136, ARG 76 (charged+); ASP 49, ASP 73, GLU 50 (charged−); GLY 77, GLY 117, GLY 119
10c	−5.821	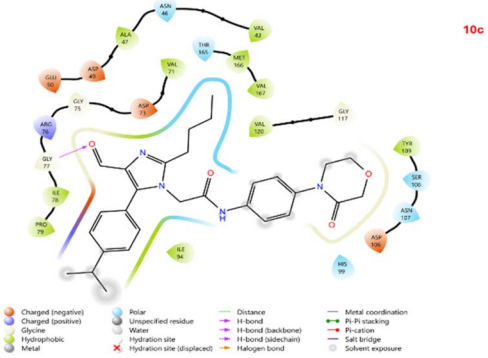	VAL 43, ALA 47, VAL 71, ILE 78, PRO 79, ILE 94, MET 166, VAL 167, VAL 120, TYR 109, ASN 46, THR 165, HIS 99, SER 108, ASN 107	ARG 76 (backbone)	ARG 76 (charged+); ASP 49, ASP 73, GLU 50, ASP 106 (charged−); GLY 75, GLY 77, GLY 117

Table 2 (*Contd.*)

Escherichia coli DNA gyrase subunit B (GyrB24) (7P2M)

Compound code	Docking score (kcal mol^{-1})	Docking image	Hydrophobic interactions/ Polar interactions	H-bond interactions	Others (charged/GLY)
10d	−5.546	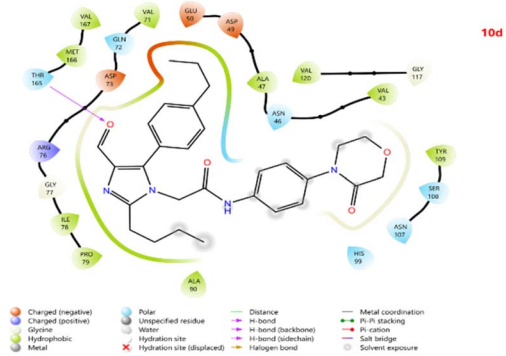	VAL 71, VAL 43, ALA 47, MET 166, VAL 167, ILE 78, PRO 79, ALA 90, VAL 120, TYR 109, THR 165, ASN 46, GLN 72, HIS 99, SER 108, ASN 107	THR 165 (backbone)	ARG 76 (charged+); ASP 49, ASP 73, GLU 50 (charged−); GLY 77, GLY 117
10e	−5.382	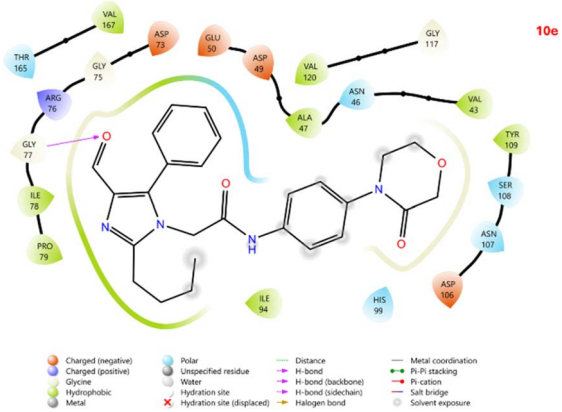	VAL 167, VAL 43, ALA 47, VAL 120, ILE 78, PRO 79, ILE 94, TYR 109, THR 165, ASN 46, HIS 99, SER 108, ASN 107	ARG 76 (backbone)	ARG 76 (charged+); ASP 49, ASP 73, GLU 50, ASP 106 (charged−); GLY 75, GLY 77, GLY 117
Novobiocin	−5.192	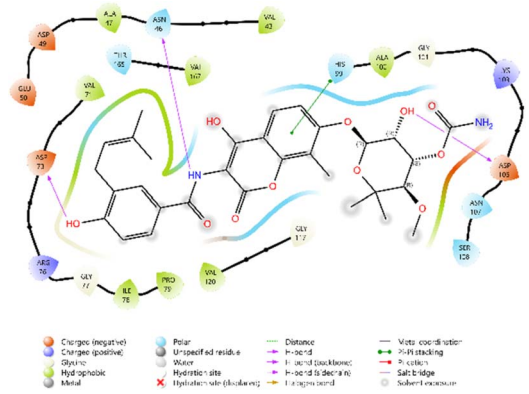	VAL 43, ALA 47, VAL 71, ILE 78, PRO 79, ALA 100, VAL 120, VAL 167	ASN 46 (sidechain), ASP 73 (side chain) ASP 106 (sidechain)	ARG 76, LYS 103 (charged+); ASP 49, GLU 50, ASP 73, (charged−)

Table 3 *In vitro* antimicrobial activity (MIC, μg mL^{-1}) of compounds **10a–e** against bacterial strains (*S. aureus*, *S. pyogenes*, *E. coli*, *P. aeruginosa*) and fungal strains (*C. albicans*, *A. niger*); chloramphenicol and griseofulvin used as reference standards

Compound	*S. aureus* MTCC 96 (μg mL^{-1})	*S. pyogenes* MTCC 442 (μg mL^{-1})	*E. coli* MTCC 443 (μg mL^{-1})	*P. aeruginosa* MTCC 1688 (μg mL^{-1})	*C. albicans* MTCC 227 (μg mL^{-1})	*A. niger* MTCC 282 (μg mL^{-1})
10a	15.62 ± 0.3	62.5 ± 0.5	31.25 ± 0.6	7.82 ± 0.4	31.25 ± 0.1	62.5 ± 0.3
10b	31.25 ± 0.4	15.62 ± 0.5	62.5 ± 0.5	31.25 ± 0.4	62.5 ± 0.1	31.25 ± 0.2
10c	7.81 ± 0.2	7.82 ± 0.7	15.62 ± 0.3	15.62 ± 0.3	15.62 ± 0.3	31.25 ± 0.5
10d	15.62 ± 0.6	15.62 ± 0.1	31.25 ± 0.3	31.25 ± 0.5	62.5 ± 0.7	62.5 ± 0.1
10e	15.62 ± 0.8	31.25 ± 0.3	31.25 ± 0.2	62.5 ± 0.5	62.5 ± 0.2	62.5 ± 0.3
Chloramphenicol	7.8 ± 0.1	7.8 ± 0.1	7.8 ± 0.2	7.8 ± 0.2	—	—
Griseofulvin	—	—	—	—	15.62 ± 0.4	15.62 ± 0.2

Table 4 DFT-optimised ground-state structures and frontier molecular orbital energies (HOMO, LUMO; eV) of compounds **10a–e** computed at the B3LYP/6-311++G(d,p) level of theory

Compound	10a	10b	10c	10d	10e
Optimized Structures	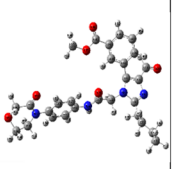	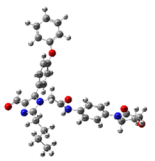	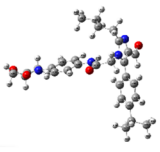	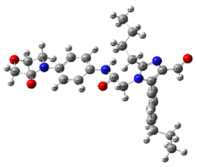	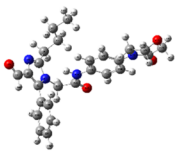
LUMO	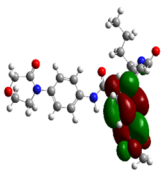 E_{LUMO} = -1.6618	 E_{LUMO} = -1.3232	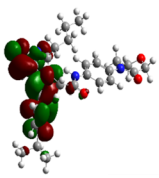 E_{LUMO} = -1.3080	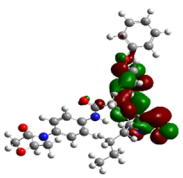 E_{LUMO} = -1.3222	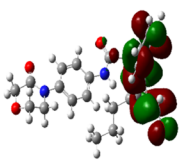 E_{LUMO} = -1.4030
HOMO	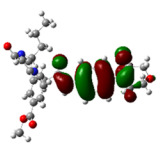 E_{HOMO} = -5.8994	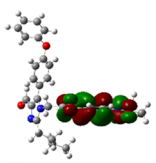 E_{HOMO} = -5.7361	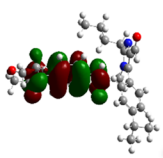 E_{HOMO} = -5.7410	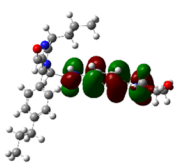 E_{HOMO} = -5.7361	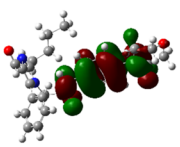 E_{HOMO} = -5.7622

both 2XCT and 7P2M, and the largest total interaction count (28 contacts). This concordance between *in silico* and *in vitro* data strongly supports DNA gyrase inhibition as the primary mechanism (Table 3).

Compound **10d**, despite having the most hydrophobic contacts in both docking targets, shows only moderate antibacterial activity (MIC 15.62–31.25 μg mL^{-1}) and weak antifungal potency, suggesting that excessive hydrophobicity without complementary polar contacts may reduce solubility or membrane permeability in cellular assays. Compound **10b** presents an intermediate profile, with moderately strong docking scores and variable MIC values, consistent with a substituent that enhances hydrophobic packing but weakens H-bond complementarity relative to **10c**.

DFT calculations

Density functional theory (DFT) calculations were performed at the B3LYP/6-311++G(d,p) level of theory using the Gaussian 16 software package. Geometry optimisations were carried out without symmetry constraints, and all optimised structures were confirmed as true energy minima by frequency analysis; no imaginary frequencies were observed. The electronic, reactivity, and thermodynamic properties derived from these calculations provide a rigorous quantum-mechanical foundation for interpreting the docking interactions and antimicrobial outcomes.

Molecular geometry optimization

The optimised geometries of all five compounds reveal stable, well-defined three-dimensional conformations in their ground states. The heterocyclic core scaffold adopts a largely planar arrangement in each compound, consistent with extended π-

conjugation across the ring system, while substituent groups introduce non-planarity through steric interactions and flexible torsion angles. The rotational constants (Table 6) confirm increasing molecular compactness in the order **10e** > **10a** > **10c** ≈ > **10b** ≈ > **10d** along the principal axis, consistent with the MW trend, and demonstrate that **10e** is the most geometrically compact compound in the series. The planar cores facilitate face-to-face hydrophobic stacking with aromatic residues (TRP 592, PHE 1097, PHE 1110) in the DNA gyrase binding pocket, a key feature of the docking poses observed across all compounds (Table 4).

Frontier molecular orbital analysis

The frontier molecular orbital energies (E_{HOMO} and E_{LUMO}) and the HOMO–LUMO energy gap (ΔE) are principal indicators of a molecule's chemical reactivity and kinetic stability. Across the series, HOMO energies span a narrow range (−5.90 to −5.74 eV), while LUMO energies range from −1.66 to −1.31 eV, yielding energy gaps (ΔE) between 4.24 and 4.43 eV.

Compound **10a** possesses the smallest ΔE (4.2376 eV), indicating the highest chemical reactivity and greatest polarisability within the series. This is consistent with its markedly elevated dipole moment (12.037 D), which far exceeds those of all other compounds (3.78–4.43 D), reflecting strong intramolecular charge separation likely arising from specific electron-withdrawing substituent effects. The high polarisability of **10a** may account for its distinctive activity profile, notably its excellent potency against *P. aeruginosa* (MIC 7.82 μg mL^{-1}), with electrostatic orientation within the outer membrane barrier potentially facilitating entry.

Compound **10c** exhibits the largest HOMO–LUMO gap (4.433 eV), denoting maximum kinetic stability and selectivity. A larger ΔE implies greater resistance to non-specific electronic perturbations and charge-transfer-mediated degradation, making **10c** more robust under physiological conditions. Crucially, this increased electronic stability does not compromise binding affinity; rather, it promotes selective and directional interactions with the gyrase active site, as evidenced by **10c** achieving the strongest docking scores against both 2XCT (−6.533 kcal mol^{-1}) and 7P2M (−5.821 kcal mol^{-1}). Compounds **10b**, **10d**, and **10e** occupy an intermediate ΔE range (4.36–4.41 eV) consistent with their intermediate biological activities (Table 4).

Global reactivity descriptors

The global chemical reactivity descriptors derived from the frontier orbital energies *via* Koopmans' theorem provide quantitative insight into electron donation, acceptance, and resistance to deformation (Table 5).

The ionization potential (I) follows the order **10a** > **10e** > **10c** > **10b** = **10d**, confirming that **10a** is the most difficult to ionise, consistent with its deeper HOMO energy (−5.8994 eV). The electron affinity (A) order (**10a** > **10e** > **10d** > **10b** > **10c**) indicates that **10a** is the most capable electron acceptor rationalising its capacity to engage electron-rich residues in the binding pocket *via* charge-transfer interactions. The electronegativity (χ) of **10a** (3.7806 eV) significantly exceeds all other compounds (3.52–3.58 eV), further underscoring its electron-withdrawing character.

Chemical hardness (η), a measure of resistance to electronic deformation, is highest for **10c** ($\eta = 2.2165$ eV), followed closely by **10b** (2.2064), **10d** (2.2069), and **10e** (2.1796), with **10a** being the softest ($\eta = 2.1188$ eV). Higher hardness in **10c** means it resists non-specific charge transfer, favouring precise, geometry-dependent interactions—exactly the profile demanded by tight, specific active-site binding. Correspondingly, softness (S) is lowest for **10c** (0.4511 eV^{-1}) and highest for **10a** (0.4719 eV^{-1}), confirming the inverse relationship.

The electrophilicity index (ω) captures a molecule's propensity to accept electrons from nucleophilic biological targets. The order is **10a** (3.3728) > **10e** (2.9443) > **10c** (2.8688) > **10b** (2.8231) > **10d** (2.8217). Compound **10a** is the most electrophilic and potentially most reactive toward nucleophilic residues (*e.g.*, Cys, Asp, Glu) in the enzyme active site. However, excessive

Table 5 Global chemical reactivity descriptors of compounds 10a–e

Descriptor	Formula	Compound **10a** (eV)	Compound **10b** (eV)	Compound **10c** (eV)	Compound **10d** (eV)	Compound **10e** (eV)
Frontier orbital energies						
E_{HOMO}	—	−5.8994	−5.7361	−5.7410	−5.7361	−5.7622
E_{LUMO}	—	−1.6618	−1.3232	−1.3080	−1.3222	−1.4030
ΔE	$E_{LUMO} - E_{HOMO}$	4.2376	4.4129	4.433	4.4139	4.3592
Global reactivity descriptors						
Ionization potential (I)	$-E_{HOMO}$	5.8994	5.7361	5.7410	5.7361	5.7622
Electron affinity (A)	$-E_{LUMO}$	1.6618	1.3232	1.3080	1.3222	1.4030
Electronegativity (χ)	$(I + A)/2$	3.7806	3.5296	3.5245	3.5291	3.5826
Chemical potential (μ)	$-\chi$	−3.7806	−3.5296	−3.5245	−3.5291	−3.5826
Hardness (η)	$(I - A)/2$	2.1188	2.2064	2.2165	2.2069	2.1796
Softness (S)	$1/\eta$	0.4719	0.4532	0.4511	0.4531	0.4587
Electrophilicity index (ω)	$\mu^2/2\eta$	3.3728	2.8231	2.8688	2.8217	2.9443
Dipole moment (μD)	—	12.037	3.9886	4.1302	4.4341	3.77892

electrophilicity can compromise selectivity and increase off-target reactivity. The balanced electrophilicity of **10c** (ω = 2.8688) is moderate rather than extreme, supporting a selective interaction mode that aligns with its optimal docking geometry and antimicrobial potency, without raising concerns about nonspecific reactivity.

Mulliken charge distributions

Mulliken population analysis was carried out on all B3LYP/6-311++G(d,p) optimised geometries to map the partial atomic charge distribution across each molecule. The resulting charge profiles (Fig. 3) reveal pronounced charge polarisation patterns that directly rationalise the binding interactions observed in molecular docking.

Across all compounds, nitrogen atoms carry substantial negative partial charges (typically −0.4 to −0.7 e), making them the primary H-bond acceptors and sites for electrostatic interactions. The carbonyl/sulfonyl oxygen atoms display the most negative charges in the series (often approaching −0.8 to −1.0 e), consistent with their role as strong H-bond acceptors precisely the atoms that engage backbone NH groups and charged residues (ARG, LYS) in the 2XCT and 7P2M docking complexes. Aromatic and aliphatic hydrogen atoms carry small but positive partial charges (+0.1 to +0.3 e), enabling CH···π and CH···O-type interactions with hydrophobic pocket residues.

Compound **10a** displays the most pronounced charge polarisation in the series with larger negative charges on heteroatoms and greater positive charges on peripheral H atoms, entirely consistent with its exceptional dipole moment (12.037 D) and highest electronegativity (χ = 3.7806). This strong charge asymmetry explains **10a**'s four hydrogen-bond interactions in the 2XCT binding pose, the highest in the series, as the strongly polarised heteroatoms provide geometrically well-directed lone pairs for complementary H-bonding with ARG 1299, ARG 447, LYS 1270, and SER 445. Compound **10c** exhibits a more evenly distributed charge profile with strategically positioned negative centers on both the carbonyl O and the ring N atoms, supporting the multidirectional interaction network (28 contacts) identified in docking, including H-bonds, hydrophobic contacts, and charged-residue engagements across both gyrase targets.

Molecular electrostatic potential

Molecular electrostatic potential (MEP) maps, computed on the B3LYP/6-311++G(d,p) electron density surface (Fig. 4), provide an intuitive visualisation of the electrostatic reactivity landscape of each compound. The colour spectrum ranges from deep red (most negative potential, electron-rich, nucleophilic) through green/yellow (neutral) to deep blue (most positive potential, electron-deficient, electrophilic).

In all five compounds, red/orange regions are localised predominantly over the heteroatom-rich core, particularly the N and O atoms of the heterocyclic ring, carbonyl groups, and any sulfonamide/sulfonyl moieties, identifying these as the principal nucleophilic sites and H-bond acceptors. These electron-dense zones directly map onto the residues engaged in H-bonding and charged interactions in docking: the negative MEP on N/O atoms is complementary to the positively charged ARG and LYS residues in 2XCT (ARG 1299, ARG 447, LYS 1270) and 7P2M (ARG 76, ARG 136). Conversely, blue/cyan regions over the aromatic periphery and NH protons represent electrophilic zones that interact with negatively charged residues (ASP 1114, ASP 1294, ASP 73, GLU 50) through charge–dipole and electrostatic complementarity, consistent with the anionic charged interactions tabulated in the docking profiles.

Compound **10a** exhibits the most extensive and intense red zones of the series, consistent with its highest dipole moment (12.037 D) and most negative Mulliken charges. The MEP surface reveals a large, highly negative electrostatic pocket localised on one face of the molecule, which correlates with its

Fig. 3 Mulliken charge distribution maps of compounds **10a–e** computed at the B3LYP/6-311++G(d,p) level.

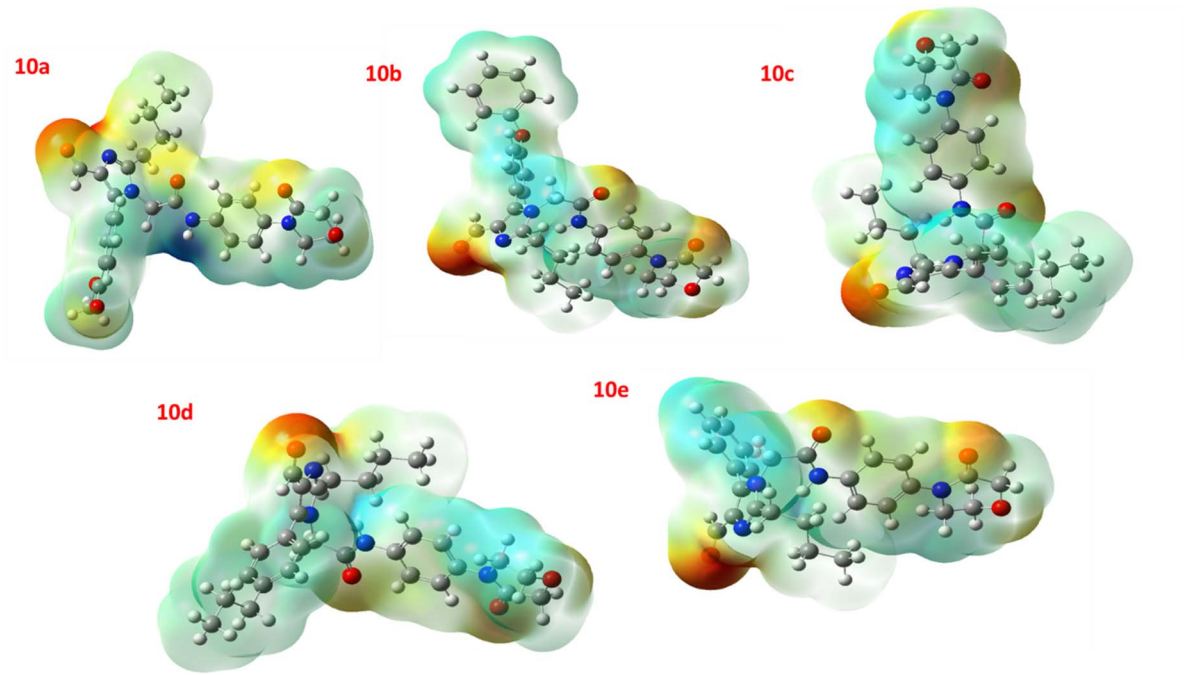

Fig. 4 Molecular electrostatic potential (MEP) maps of compounds **10a–e** plotted on the B3LYP/6-311++G(d,p) electron density surface.

four H-bond interactions in 2XCT. Compound **10c** displays a balanced, well-distributed MEP pattern, moderately electron-rich N/O centres paired with defined electron-poor aromatic sectors, producing a surface complementary to the amphipathic character of the DNA gyrase active site. This balanced electrostatic topology underpins **10c**'s ability to form simultaneous hydrophobic, H-bond, and charged interactions across a broad pocket surface, directly explaining its superior binding affinity and antimicrobial profile.

Thermodynamic parameter

The thermodynamic parameters computed at B3LYP/6-311++G(d,p) zero-point vibrational energy (ZPVE), total thermal energy (E_{total}), and partitioned translational, rotational, and vibrational contributions are compiled in Table 6.

The zero-point vibrational energies scale with molecular complexity: **10e** (321.08 kcal mol^{-1}) < **10a** (347.65) < **10b** ≈ **10c** ≈ **10d** (~374 kcal mol^{-1}). This ordering mirrors the MW trend and indicates that **10e**, with fewer atoms and bonds, has the lowest collective harmonic-oscillator ground-state energy. The total thermal energies follow the same hierarchy (**10e**: 340.36 kcal mol; **10b**: 397.48 kcal mol^{-1}, the highest), confirming that the thermochemical stability of each compound is commensurate with its structural extent.

The vibrational contribution dominates the thermal energy in all compounds (*e.g.*, **10c**: 394.84 out of 396.62 kcal mol^{-1} total; ≈99.5%), while translational and rotational contributions are uniformly 0.889 kcal mol^{-1} in all five cases in perfect agreement with the classical equipartition theorem (3/2 RT at 298.15 K ≈ 0.889 kcal mol^{-1}), confirming the physical validity of the thermodynamic calculations. The rotational constants for **10e** are the largest along the principal axis (A = 0.17422 GHz *vs.* 0.10–0.12 GHz for the others), indicating the smallest principal moment of inertia and the most compact molecular frame, consistent with **10e**'s lowest MW (460.21 Da) and lowest *n*ROTB (**10**). Collectively, these thermodynamic parameters confirm that all five compounds are thermally stable, well-converged structures with physically meaningful energetics, providing a sound computational basis for interpreting their electronic reactivity and biological properties.

ADMET study

The drug-likeness and predicted pharmacokinetic profiles of all compounds were assessed using Lipinski's Rule of Five and Veber's oral bioavailability criteria. Key descriptors, molecular weight (MW), hydrogen bond acceptors (HBA), hydrogen bond donors (HBD), calculated lipophilicity (c Log P), number of rotatable bonds (*n*ROTB), topological polar surface area (TPSA), aqueous solubility (Log S), and percentage oral absorption (% ABS) are summarised in Table 7.

All compounds (**10a–e**) satisfied Lipinski's Rule of Five with zero violations, confirming their theoretical suitability for oral administration. HBD values were uniformly low (1 across all test compounds *vs.* 3 for chloramphenicol), well within the ≤5 threshold, while HBA values ranged from 8–10, all compliant with the ≤10 limit. c Log P values spanning 2.34–4.24 indicate moderate lipophilicity, favouring passive membrane diffusion — a prerequisite for intracellular target engagement. All compounds comply with Veber's criteria (TPSA ≤ 140 Å^2; *n*ROTB ≤ 10 for **10e**, ≤12 for others), though the slightly elevated rotatable bond counts in **10a–d** (*n*ROTB 11–12) hint at moderate conformational flexibility that may influence binding

Table 6 Thermodynamic parameters of compounds **10a–e** computed at the B3LYP/6-311++G(d,p) level

Sr. No	Parameters	B3LYP 6-311 ++G (d, p) compound **10a**	B3LYP 6-311 ++G (d, p) compound **10b**	B3LYP 6-311 ++G (d, p) compound **10c**	B3LYP 6-311 ++G (d, p) compound **10d**	B3LYP 6-311 ++G (d, p) compound **10e**
1	Zero-point vibrational energy (kcal mol^{-1})	347.6526	374.6143	374.5816	374.6620	321.0817
2	Rotational temperature (K)	0.00529	0.00446	0.00560	0.00539	0.00836
		0.00213	0.00195	0.00260	0.00251	0.00287
		0.00170	0.00154	0.00210	0.00201	0.00261
3	Rotational constant (GHz)	0.11032	0.09299	0.11661	0.11230	0.17422
		0.04437	0.04063	0.05420	0.05221	0.05990
		0.03541	0.03214	0.04379	0.04181	0.05441
4	Total energy E_{total} (kcal mol^{-1})	369.925	397.477	396.618	396.735	340.357
5	Translational (kcal mol^{-1})	0.889	0.889	0.889	0.889	0.889
6	Rotational (kcal mol^{-1})	0.889	0.889	0.889	0.889	0.889
7	Vibrational (kcal mol^{-1})	368.147	395.699	394.840	394.958	338.579

Table 7 Predicted ADMET and drug-likeness parameters of compounds **10a–e**

Lipinski's rule						Vebar's rule			
Compd	Lipinski's Violations	MW[a] (≤500)	HBA[b] (≤10)	HBD[c] (≤10)	*c* Log *P*[d] (≤5)	*n*ROTB[e] (≤10)	TPSA[f] (140 Å^2)	Log *S*[g]	%ABS[h]
10a	0	518.22	10	1	2.56	12	119.83	−4.17891	67.66
10b	0	552.24	9	1	4.24	12	102.76	−5.04662	73.55
10c	0	502.26	8	1	3.75	11	93.53	−4.48741	76.74
10d	0	502.26	8	1	3.67	12	93.53	−4.40012	76.74
10e	0	460.21	8	1	2.34	10	93.53	−3.86532	76.74
Griseofulvin	0	352.07	6	0	1.88	3	71.06	−4.80481	84.49
Chloramphenicol	0	322.01	7	3	0.91	7	112.7	−2.72514	70.12

[a] Molecular weight. [b] Hydrogen bond acceptors. [c] Hydrogen bond donors. [d] Calculated partition coefficient (lipophilicity). [e] Number of rotatable bonds. [f] Topological polar surface area. [g] Logarithm of solubility. [h] Percent absorption.

pose stability, consistent with the varied docking interaction profiles observed.

A particularly notable trend emerges in TPSA and oral absorption. Compounds **10c**, **10d**, and **10e** share the lowest TPSA in the series (93.53 Å^2), and consequently the highest predicted oral absorption (%ABS = 76.74%), which is substantially better than **10a** (TPSA 119.83 Å^2; %ABS 67.66%) and **10b** (TPSA 102.76 Å^2; %ABS 73.55%). Reduced TPSA reflects a less polar molecular surface, facilitating passive paracellular and transcellular transport. This directly correlates with biological outcomes: **10c**, **10d**, and **10e** all recorded superior antibacterial MIC values against both Gram-positive organisms (*S. aureus*, *S. pyogenes*) compared with **10a** and **10b**, suggesting that higher gastrointestinal absorption translates into better bioavailability at the target site.

Compound **10c** stands out as the most drug-like candidate when all ADMET descriptors are considered holistically. Its MW of 502.26 Da is the lowest in the **10c**/**10d** pair and well within acceptable boundaries; its *c* Log *P* of 3.75 sits in the optimal window (2–4) for both membrane permeability and aqueous solubility, avoiding the excess lipophilicity seen in **10b** (*c* Log *P* 4.24, Log *S* −5.05 the least soluble compound) while providing sufficient hydrophobicity to engage the largely hydrophobic ATP-binding cleft of DNA gyrase, as confirmed by its 14 hydrophobic residue contacts in 2XCT. Its Log *S* of −4.49 indicates moderate aqueous solubility, supporting systemic distribution, while its *n*ROTB of 11 offers enough flexibility to adopt the binding conformation identified in docking yet retains sufficient rigidity (*vs.* the higher-entropy **10a** and **10b**) to limit entropic binding penalties. Collectively, **10c** achieves the ideal balance: high predicted absorption (76.74%), optimal lipophilicity, good solubility, and zero drug-likeness violations, properties that translate directly into its superior docking affinity and *in vitro* antimicrobial potency.

By contrast, compounds **10a** and **10b** exhibit pharmacokinetic liabilities despite having no Lipinski violations. Compound **10b** carries the highest MW (552.24 Da) and *c* Log *P* (4.24) of the series alongside the poorest predicted solubility

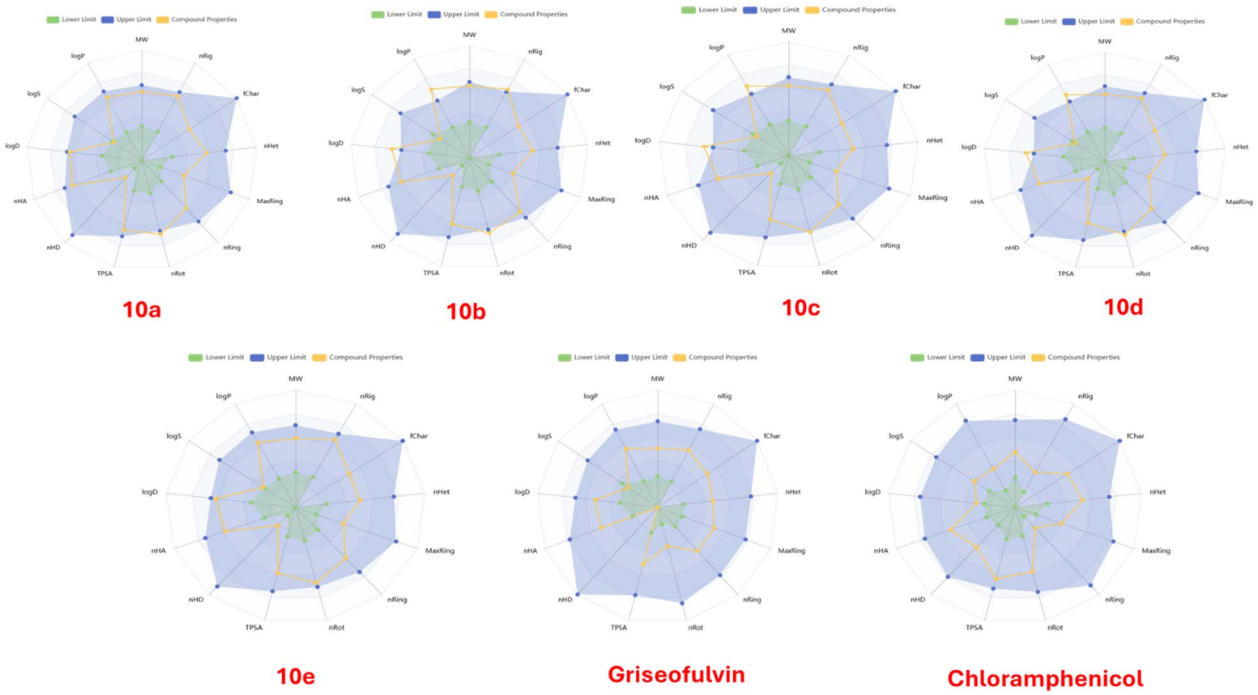

Fig. 5 Radar (spider) plots illustrating the predicted ADMET and drug-likeness profiles of compounds **10a–e**.

(Log *S* −5.05), which likely contributes to its inconsistent MIC values across organisms particularly its weak activity against *E. coli* (62.5 μg mL^{-1}) where membrane penetration of the outer leaflet is critical. Compound **10a**, with the highest TPSA (119.83 $Å^2$) and lowest absorption (67.66%), may experience reduced intracellular accumulation, dampening its *in vivo* potential despite a reasonable docking score (−5.308 kcal mol^{-1}, 2XCT). Compound **10e**, while offering the lowest MW (460.21 Da), lowest *n*ROTB (10 fully Veber-compliant), and best Log *S* (−3.87, most soluble), is limited by a moderate *c* Log *P* (2.34) that may reduce lipid bilayer partitioning relative to **10c**, consistent with its weaker docking scores against both targets (Fig. 5).

Experimental section

All reagents and solvents were purchased from commercial suppliers (Sigma-Aldrich, TCI, and Spectrochem) and used without further purification unless otherwise stated. Valeronitrile, glycine, chloroacetyl chloride, potassium carbonate, phosphorus oxychloride, DMF, arylboronic acids, and $PdCl_2$(dppf) were of reagent grade. Anhydrous methanol, dry acetone, acetonitrile, toluene, and ethyl acetate were used as received or freshly dried where required.

Melting points were determined on a Thermo Scientific melting point apparatus and are uncorrected. ^1H and ^{13}C NMR spectra were recorded on a Bruker Avance 400 MHz spectrometer using DMSO-d_6 as solvent with TMS as internal reference; chemical shifts are reported in δ (ppm) and coupling constants (J) in Hz. IR spectra were acquired on a PerkinElmer ATR–FTIR spectrometer ($\tilde{\nu}$ in cm^{-1}). High-resolution mass spectra (HR-ESI-MS) were recorded on a Waters Synapt G2 Q-TOF mass spectrometer in positive-ion mode. Reaction progress was monitored by TLC on pre-coated silica gel 60 F_{254} aluminium sheets (Merck), visualised under UV light (254/365 nm). Column chromatography was performed on silica gel (60–120 mesh) using ethyl acetate/hexane as eluent.

Synthesis of methyl pentanimidate (2)

Valeronitrile (100 g, 1.20 mol) was dissolved in anhydrous methanol (58 mL), and the solution was cooled to −5 to −10 °C under stirring. Dry hydrogen chloride gas was bubbled through the reaction mixture for 15–18 h while maintaining the temperature below −5 °C. After saturation, additional methanol (55 mL) was added, and the reaction mixture was stirred for a further 1 h at the same temperature. The resulting solution was then cautiously transferred into a methanolic ammonia solution (12–15 wt%) under stirring, maintaining the temperature at 20–30 °C and the pH in the range of 8–9. The mixture was stirred for 3 h, during which inorganic salts precipitated. The precipitate was removed by filtration and washed with methanol (25 mL). The combined filtrate was concentrated under reduced pressure (≤90 °C) until the methanol was completely removed. The crude product was obtained as a semi-solid and used without further purification.

Synthesis of 2-butyl-5-chloro-3*H*-imidazole-4-carbaldehyde (4)

Glycine (50 g, 0.666 mol) was added portion-wise to a freshly prepared solution of sodium hydroxide (26.64 g, 0.666 mol) in methanol (250 mL) at 0 °C. The mixture was stirred for 15 min to form a homogeneous suspension. Methyl pentanimidate (80 g, 0.70 mol) was added dropwise over 10–15 min at 0–5 °C. The reaction mixture was then allowed to warm to room temperature and stirred for 16 h. The solvent was removed

under reduced pressure below 50 °C. The residue was diluted with toluene (500 mL), followed by the dropwise addition of phosphorus oxychloride (320 g, 2.08 mol) over 1 h at controlled temperature. Subsequently, *N*,*N*-dimethylformamide (150 g, 2.05 mol) was added over 2 h. The reaction mixture was heated at 100 °C for 2 h. After cooling to ~30 °C, the reaction mixture was cautiously quenched with chilled deionized water (260 mL), maintaining the temperature below 25 °C. The mixture was treated with filter aid (30 g), and the pH was carefully adjusted to ~1–2 (corrected) using aqueous sodium hydroxide solution. The mixture was filtered, and the organic layer was separated. The toluene phase was washed with water (2 × 400 mL), treated with activated charcoal (8 g), stirred at 30–35 °C for 30 min, and filtered. The filtrate was concentrated under reduced pressure below 55 °C to approximately half its volume and cooled to 0–5 °C to induce crystallization. The precipitated solid was filtered, washed with cold toluene (25 mL), and dried at 50–55 °C to constant weight.

Synthesis of 2-chloro-*N*-(4-(3-oxomorpholino)phenyl) acetamide (7)

A solution of 4-(4-aminophenyl)morpholin-3-one (1.0 equiv.) in dry acetone was cooled to 0 °C. Chloroacetyl chloride (1.1 equiv.) was added dropwise under stirring, maintaining the temperature at 0–5 °C. The reaction mixture was stirred for 2–3 h at the same temperature. Upon completion (monitored by TLC), the reaction mixture was poured onto crushed ice. The resulting precipitate was filtered, washed thoroughly with water to remove residual acid, and dried under vacuum. The crude product was used directly in the next step without further purification.

Synthesis of 2-(2-butyl-5-chloro-4-formyl-1*H*-imidazol-1-yl)-*N*-(4-(3-oxomorpholino) phenyl) acetamide (8)

To a stirred solution of intermediate 7 (1.0 equiv.) in acetonitrile (2 V) was added intermediate 4 (1.0 equiv.), followed by potassium carbonate (1.2 equiv.). The reaction mixture was stirred at room temperature for 10–15 min and then heated to reflux for 3–4 h. The progress of the reaction was monitored by TLC. After completion, the reaction mixture was cooled to room temperature and the precipitated solid was collected by filtration. The solid was washed with cold acetonitrile, followed by water, and dried under vacuum to afford the desired product.

General procedure for the synthesis of compounds (10a–e)

A mixture of intermediate 8 (1.0 equiv.), substituted aryl boronic acid (1.1 equiv.), and potassium carbonate (3.0 equiv.) was dissolved in a methanol–water mixture (8 : 2). The reaction mixture was degassed (recommended improvement) and $PdCl_2$(dppf) (0.1 equiv.) was added under an inert atmosphere. The reaction mixture was heated at 100 °C for 3–4 h with continuous stirring. After completion (monitored by TLC), the reaction mixture was cooled and poured onto crushed ice. The product was extracted with ethyl acetate (3×). The combined organic layers were dried over anhydrous sodium sulfate and concentrated under reduced pressure. The crude product was purified by column chromatography using ethyl acetate/hexane (9 : 1) as eluent to afford the desired compounds (**10a–e**).

Spectral data

*Methyl 3-(2-butyl-4-formyl-1-(2-oxo-2-((4-(3-oxomorpholino) phenyl)amino)ethyl)-1H-imidazol-5-yl) benzoate (**10a**).* Grey solid; yield 82%; m. p. 200–202 °C; $C_{28}H_{30}N_4O_6$ (518.57 g mol^{-1}). ^{1}H NMR (400 MHz, DMSO-d_6) in δ ppm: 10.49 (s, 1H, –CONH–), 9.75 (s, 1H, –CHO), 8.29 (s, 1H, Ar–H), 8.02–8.04 (d, 2H, J = 8 Hz, Ar–H), 7.61–7.66 (m, 3H, Ar–H), 7.33–7.35 (d, 2H, J = 8 Hz, Ar–H), 5.25 (s, 2H, –CH_2–), 4.18 (s, 2H, –CH_2–), 3.94–3.96 (d, 2H, J = 8 Hz, –CH_2–), 3.71 (d, 3H, J = 8 Hz, –OCH_3), 3.68–3.69 (d, 2H, J = 4 Hz –CH_2–), 2.75–2.79 (t, 2H, J = 8 Hz, –CH_2–), 1.68–1.76 (q, 2H, –CH_2–), 1.36–1.41 (m, 2H, –CH_2–), 0.91–0.93 (t, 3H, J = 8 Hz, –CH_3). ^{13}C NMR (100 MHz, DMSO-d_6): δ = 180.43 (C=O, morpholine carbonyl), 166.43 (C=O, ester), 165.84 (C=N, imidazole), 165.29, 156.20 (aromatic C–O), 155.84, 151.44 (aromatic C–N), 137.43, 137.35 (aromatic C), 133.58, 133.52, 133.29 (aromatic C), 129.79, 129.29 (aromatic CH), 68.20, 63.96 (OCH_2, morpholine), 52.10 (OCH_3), 49.51 (NCH_2), 43.41 (NCH_2, morpholine), 40.01, 30.50, 29.94 (CH_2), 25.94 (CH_2), 19.80 ppm (CH_3). IR (ATR–FTIR): $\hat{\nu}$_max = 3273 (N–H str), 2959 (C–H str), 1719 (C=O, ester), 1690 (C=O, amide), 1655 (C=O, morpholine), 1610, 1551, 1514 (C=C/C=N, ar), 1466, 1356, 1327 (C–H bend), 1273, 1237 (C–O–C str), 1126, 992, 841, 720 cm^{-1}. HR-ESI-MS (+): m/z = 519.2252 $[M + H]^+$ (calcd for $C_{28}H_{31}N_4O_6$: 519.2238; Δ = 2.56 ppm); 536.2383 $[M + NH_4]^+$; 541.2066 $[M + Na]^+$; 557.1806 $[M + K]^+$.

*2-(2-Butyl-4-formyl-5-(4-phenoxyphenyl)-1H-imidazol-1-yl)-N-(4-(3-oxomorpholino) phenyl)acetamide (**10b**).* Ivory solid; yield 78%; m. p. 194–196 °C; $C_{32}H_{32}N_4O_5$ (552.63 g mol^{-1}). ^{1}H NMR (400 MHz, DMSO-d_6) in δ ppm: 10.50 (s, 1H, –CONH–), 9.73 (s, 1H, –CHO), 7.76–7.78 (d, 2H, J = 8 Hz, Ar–H), 7.61–7.63 (d, 2H, J = 8 Hz, Ar–H), 7.43–7.44 (t, 2H, J = 4 Hz Ar–H), 7.34–7.36 (d, 2H, J = 8 Hz, Ar–H), 7.21 (s, 1H, Ar–H), 7.08–7.13 (m, 4H, Ar–H), 5.25 (s, 2H, –CH_2–), 4.19 (s, 2H, –CH_2–), 3.97 (s, 2H, –CH_2–), 3.71 (s, 2H, –CH_2–), 2.75–2.77 (t, 2H, J = 8 Hz, –CH_2–), 1.70–1.74 (t, 2H, J = 8 Hz, –CH_2–), 1.38–1.44 (q, 2H, –CH_2–), 0.90–0.93 (t, 3H, J = 8 Hz, –CH_3). ^{13}C NMR (100 MHz, DMSO-d_6): δ = 180.44 (C=O, morpholine), 166.38, 166.37, 166.24 (C=O and C=N, overlapping), 156.04 (aromatic C–O), 152.47 (aromatic C–N), 137.39, 134.66 (aromatic C), 131.66, 128.59 (aromatic C), 126.59, 126.40 (aromatic CH), 119.75, 119.69, 118.69 (aromatic CH, diphenyl ether region), 68.20, 63.96 (OCH_2), 49.51, 48.40 (NCH_2), 40.61, 39.57 (CH_2), 25.22, 22.28 (CH_2), 14.20 ppm (CH_3). IR (ATR–FTIR): $\hat{\nu}$_max = 3294 (N–H str), 2957 (C–H str), 1647 (C=O str), 1545, 1488 (C=C ar), 1464, 1392, 1326, 1252, 1233 (C–O–C str, phenoxy), 1163, 1123, 1102, 837, 746, 689, 662, 629 cm^{-1}. HR-ESI-MS (+): m/z = 553.2474 $[M + H]^+$ (calcd for $C_{32}H_{33}N_4O_5$: 553.2445; Δ = 4.98 ppm); 575.2287 $[M + Na]^+$; 591.2031$[M + K]^+$.

*2-(2-Butyl-4-formyl-5-(4-isopropylphenyl)-1H-imidazol-1-yl)-N-(4-(3-oxomorpholino) phenyl)acetamide (**10c**).* Off-white solid; yield 89%; m. p. 198–200 °C; $C_{29}H_{34}N_4O_4$ (502.61 g mol^{-1}). ^{1}H NMR (400 MHz, DMSO-d_6) in δ ppm: 10.48 (s, 1H, –CONH–), 9.71 (s, 1H, –CHO), 7.59–7.64 (m, 4H, Ar–H), 7.35 (s, 4H, Ar–H), 5.23 (s, 2H, –CH_2–), 4.18 (s, 2H, –CH_2–), 3.95 (s, 2H, –CH_2–), 3.69 (s, 2H, –CH_2–), 2.95 (s, 1H, –CH–), 2.73 (s, 2H, –CH_2–), 1.71 (s, 2H, –CH_2–), 1.40 (s, 2H, –CH_2–), 1.23–1.25 (d, 6H, J = 8 Hz, –

CH_3), 0.90 (s, 3H, –CH_3). ^{13}C NMR (100 MHz, DMSO-d_6): δ = 180.47 (C=O, morpholine), 166.38 (C=N/C=O), 165.75 (C=O), 156.03, 155.23 (aromatic C–N), 143.46 (aromatic C bearing isopropyl), 137.39 (aromatic C), 131.64, 128.59, 128.22, 126.62, 126.29 (aromatic CH), 68.20, 63.96 (OCH_2), 49.51 (NCH_2), 33.82 (CH of isopropyl), 29.51 (CH_2), 23.78 (CH_3, isopropyl × 2), 22.28 (CH_2), 13.90 ppm (terminal CH_3). IR (ATR–FTIR): $\hat{\nu}$_max = 3313 (N–H str), 2954, 2866 (C–H str, isopropyl CH), 1688, 1644 (C=O str), 1607, 1548, 1514 (C=C/C=N ar), 1464, 1430, 1392, 1352, 1326 (C–H bend), 1264, 1236, 1187, 1163, 1123 (C–O–C str), 1022, 994, 873, 835, 699, 663, 635 cm^{-1}. HR-ESI-MS (+): m/z = 503.2681 $[M + H]^+$ (calcd for $C_{29}H_{35}N_4O_4$: 503.2658; Δ = 5.03 ppm); 525.2483 $[M + Na]^+$; 541.2252 $[M + K]^+$.

*2-(2-Butyl-4-formyl-5-(4-propylphenyl)-1H-imidazol-1-yl)-N-(4-(3-oxomorpholino) phenyl)acetamide (**10d**).* Off-white solid; yield 86%; m. p. 208–210 °C; $C_{29}H_{34}N_4O_4$ (502.61 g mol^{-1}). ^{1}H NMR (400 MHz, DMSO-d_6) in δ ppm: 10.47 (s, 1H, –CONH–), 9.71 (s, 1H, –CHO), 7.59–7.63 (m, 4H, Ar–H), 7.31 (s, 4H, Ar–H), 5.23 (s, 2H, –CH_2–), 4.18 (s, 2H, –CH_2–), 3.95 (s, 2H, –CH_2–), 3.69 (s, 2H, –CH_2–), 2.73 (s, 2H, –CH_2–), 2.61 (s, 2H, –CH_2–), 1.62–1.64 (d, 4H, J = 8 Hz, –CH_2–), 1.39 (s, 2H, –CH_2–), 0.90–0.92 (d, 6H, J = 8 Hz, –CH_3). ^{13}C NMR (100 MHz, DMSO-d_6): δ = 180.47 (C=O, morpholine), 166.38 (C=N/C=O), 165.76 (C=O), 146.22 (aromatic C bearing n-propyl), 137.40 (aromatic C), 130.42, 128.59, 128.22, 127.63 (aromatic C/CH), 68.20, 63.96 (OCH_2), 49.51 (NCH_2), 37.49, 24.63, 22.63 (propyl CH_2 chain), 19.77 ppm (terminal CH_3). IR (ATR–FTIR): $\hat{\nu}$_max = 2959 (C–H str), 1649 (C=O str), 1607, 1550, 1509 (C=C ar), 1465, 1415, 1325 (C–H bend), 1119 (C–O–C str), 843, 667 cm^{-1}. HR-ESI-MS (+): m/z = 503.2678 $[M + H]^+$ (calcd for $C_{29}H_{35}N_4O_4$: 503.2658; Δ = 4.60 ppm); 502.2534 M^+; 525.2486 $[M + Na]^+$; 541.2228 $[M + K]^+$.

*2-(2-Butyl-4-formyl-5-phenyl-1H-imidazol-1-yl)-N-(4-(3-oxomorpholino)phenyl) acetamide (**10e**).* Brown solid; yield 80%; m. p. 204–206 °C; $C_{26}H_{28}N_4O_4$ (460.53 g mol^{-1}). ^{1}H NMR (400 MHz, DMSO-d_6) in δ ppm: 10.49 (s, 1H, –CONH–), 9.72 (s, 1H, –CHO), 7.74 (s, 2H, Ar–H), 7.59–7.61 (d, 2H, J = 8 Hz, Ar–H), 7.48–7.50 (d, 3H, J = 8 Hz, Ar–H), 7.33–7.35 (d, 2H, J = 8 Hz, Ar–H), 5.24 (s, 2H, –CH_2–), 4.18 (s, 2H, –CH_2–), 3.96–3.98 (d, 2H, J = 8 Hz, –CH_2–), 3.70–3.72 (d, 2H, J = 8 Hz, –CH_2–), 1.96–1.99 (t, 2H, J = 8 Hz, –CH_2–), 1.86–1.92 (q, 2H, –CH_2–), 1.70–1.73 (t, 2H, J = 8 Hz, –CH_3), 1.43 (s, 3H, –CH_3). ^{13}C NMR (100 MHz, DMSO-d_6): δ = 180.56 (C=O, morpholine), 166.38 (C=N/C=O), 165.72 (C=O), 156.07, 155.06 (aromatic C–N), 137.39 (aromatic C), 128.59, 128.22, 127.63 (aromatic CH), 68.20, 63.96 (OCH_2), 49.51 (NCH_2), 40.01, 29.78 (CH_2), 25.92 (CH_2), 22.28 (CH_2), 14.20 ppm (terminal CH_3). IR (ATR–FTIR): $\hat{\nu}$_max = 2925 (C–H str), 1692, 1641 (C=O str), 1610, 1551, 1508 (C=C/C=N ar), 1470, 1428, 1397, 1308 (C–H bend), 1238, 1124 (C–O–C str), 841, 748, 718, 700, 671 cm^{-1}. HR-ESI-MS (+): m/z = 461.2203 $[M + H]^+$ (calcd for $C_{26}H_{29}N_4O_4$: 461.2189; Δ = 4.23 ppm); 483.2020 $[M + Na]^+$; 499.1778 $[M + K]^+$.

Conclusion

This study reports the design, synthesis, and comprehensive evaluation of five novel imidazole–morpholinone hybrids (**10a–e**) as broad-spectrum antimicrobial agents. The convergent five-step synthetic route, employing Vilsmeier–Haack cyclisation, regioselective *N*-alkylation, and Pd-catalysed Suzuki–Miyaura cross-coupling, provided efficient access to structurally diverse analogues with yields of 45–89%.

Compound **10c**, bearing a 4-isopropylphenyl substituent at C5 of the imidazole, emerged as the standout lead across all evaluation parameters. It matched the antibacterial activity of chloramphenicol against both *S. aureus* and *S. pyogenes* (MIC 7.81–7.82 μg mL^{-1}) and equalled griseofulvin's antifungal potency against *C. albicans* and *A. niger* (MIC 15.62 μg mL^{-1}), making it the sole compound to achieve reference-level activity across both Gram-positive and Gram-negative organisms. This biological superiority was strongly corroborated by molecular docking, where **10c** recorded the highest binding affinities against both *S. aureus* DNA gyrase (2XCT: −6.533 kcal mol^{-1}) and *E. coli* GyrB24 (7P2M: −5.821 kcal mol^{-1}), forming an extensive 28-contact interaction network.

DFT analysis revealed that **10c** possesses the largest HOMO–LUMO gap (4.433 eV), conferring maximum kinetic stability and selectivity, while Mulliken charge and MEP analyses confirmed balanced electrostatic complementarity to the gyrase active site. ADMET profiling further validated **10c** as the most drug-like candidate, satisfying all Lipinski and Veber criteria with optimal lipophilicity (c Log P 3.75), moderate aqueous solubility (Log S −4.49), and the highest predicted oral absorption (76.74%) in the series.

Collectively, these findings establish compound **10c** as a high-priority lead for further optimisation and preclinical investigation in the quest for new antimicrobial chemotypes.

Conflicts of interest

There are no conflicts to declare.

Data availability

Supplementary information (SI): NMR, FT-IR, mass spectra, computational DFT files, molecular docking results, and ADME analysis. Additional raw data can be made available from the corresponding author upon reasonable request. See DOI: https://doi.org/10.1039/d6ra03352k.

References

1 C. J. L. Murray, K. S. Ikuta, F. Sharara, L. Swetschinski, G. Robles Aguilar, A. Gray and M. Naghavi, *The Lancet*, 2022, **399**, 629–655.
2 GBD 2021 Antimicrobial Resistance Collaborators, *The Lancet*, 2024, **404**, 1199–1226.
3 C. S. Ho, C. T. H. Wong, T. T. Aung, R. Lakshminarayanan, J. S. Mehta and S. Rauz, *Lancet Microbe*, 2024, **5**, 100947.
4 S. S. Joshi, A. J. Dave, J. B. Maheta, Y. O. Bhola and J. Upadhyay, *J. Mol. Struct.*, 2026, **1369**, 146343.
5 G. B. Patel, Y. O. Bhola, P. V. Dholaria, A. R. Suthar and D. M. Bhatt, *Future Med. Chem.*, 2026, 1–12, DOI: 10.1080/17568919.2026.2669609.

6 A. Štimac, M. Šekutor, K. Mlinarić-Majerski, L. Frkanec and R. Frkanec, *Int. J. Mol. Sci.*, 2024, **25**, 9503.
7 E. Kabir and M. Uzzaman, *Results Chem.*, 2022, **4**, 100606.
8 J. B. Maheta, D. K. Lakhnotra, N. H. Shaikh, P. A. Dave, D. Pathak, S. B. Koradiya and Y. O. Bhola, *J. Mol. Struct.*, 2025, **1354**, 144824.
9 A. Chavda, B. B. Makwana, J. B. Maheta, U. P. Tarpada and Y. O. Bhola, *J. Mol. Struct.*, 2026, **1370**, 146454.
10 M. Ghara, M. El-Naggar, I. Ranđelović, T. Takács, J. Tóvári and A. Csámpai, *Molecules*, 2025, **30**, 2245.
11 K. Kushwaha, M. Chaudhary, S. Soni, R. Kharb and A. Chauhan, *ChemistrySelect*, 2025, **10**, e202502943.
12 P. Kamboj, A. Mahore, A. Husain, M. Shaquiquzzaman, M. M. Alam and M. Amir, *Mini-Rev. Med. Chem.*, 2023, **23**, 1733–1759.
13 D. K. Lakhnotra, J. B. Maheta, Y. O. Bhola, B. N. Socha, N. H. Shaikh, P. A. Dave and S. B. Koradiya, *RSC Adv.*, 2026, **16**, 6314–6337.
14 N. Singh, A. Pandurangan, K. Rana, P. Anand, A. Ahmad and A. K. Tiwari, *Bioorg. Chem.*, 2020, **97**, 103650.
15 S. Meninno and A. Lattanzi, *J. Org. Chem.*, 2023, **88**, 7888–7892.
16 J. Magano and J. R. Dunetz, *J. Organomet. Chem.*, 2022, **976**, 122438.
17 M. V. Santos, S. V. Rios-Londoño and D. Becerra, *Molecules*, 2020, **25**, 3493.
18 T. Wan, L. Capaldo, J. Djossou, A. Staffa, F. J. de Zwart, B. de Bruin and T. Noël, *Nat. Commun.*, 2024, **15**, 3926.
19 N. H. Shaikh, J. B. Maheta, D. K. Lakhnotra, I. M. Ram, Y. O. Bhola and S. A. Jain, *ChemistrySelect*, 2025, **10**, e202503975.
20 N. Sinha, S. Srivastava and S. K. Garg, *Biomedicines*, 2023, **11**, 371.
21 M. Salman, P. Sharma, M. Kumar, A. S. Ethayathulla and P. Kaur, *Briefings Funct. Genomics*, 2023, **22**, 180–194.
22 M. M. C. Buckner, S. Pennington, R. Summers and J. D. Blande, *Pharmaceuticals*, 2023, **16**, 261.
23 D. V. Pathak, J. B. Maheta, D. K. Lakhnotra, Y. O. Bhola, H. A. Modi, P. D. Suradiya, D. B. Chhag, A. K. Mahida and G. L. Jadav, *Polycyclic Aromat. Compd.*, 2026, 1–18.
24 I. M. Ram, J. B. Maheta, D. K. Lakhnotra, N. H. Shaikh, V. U. Majethiya and Y. O. Bhola, *Synth. Commun.*, 2026, 1–28.
25 A. H. Abdelazeem, A. M. M. El-Saghier, W. M. El-Husseiny, A. M. Kadry and H. A. Omar, *Drug Dev. Res.*, 2022, **83**, 761–802.
26 D. Katariya, C. Gori, P. Solanki, B. Kataria and R. Khunt, *Lett. Org. Chem.*, 2025, **23**, 61–70.
27 A. J. Dave, S. S. Joshi, B. B. Makwana, H. A. Parmar, P. N. Chauhan and J. Upadhyay, *ChemistrySelect*, 2026, **11**, e202505650.